Crack bridging in as-fabricated and embrittled tungsten single fibre-reinforced tungsten composites shown by a novel in-situ high energy synchrotron tomography bending test

J. Riesch, J. -Y. Buffiere, T. Hoeschen, M. Scheel, Ch. Linsmeier, J. -H. You

Nuclear Materials and Energy 15 (2018) 1–12

Contents lists available at ScienceDirect

Nuclear Materials and Energy

journal homepage: www.elsevier.com/locate/nme

Crack bridging in as-fabricated and embrittled tungsten single fibre-reinforced tungsten composites shown by a novel in-situ high energy synchrotron tomography bending test

J. Riesch[*,a], J.-Y. Buffiere[b], T. Höschen[a], M. Scheel[c,d], Ch. Linsmeier[e], J.-H. You[a]

[a] Max-Planck-Institut für Plasmaphysik, 85748 Garching, Germany
[b] MATEIS INSA Lyon, 20 Av. A. Einstein, 69621 Villerbanne, Cedex, France
[c] ESRF-The European Synchrotron Radiation, 71 Av. des Martyrs, Grenoble 38000, France
[d] Synchrotron Soleil, L'Orme des Merisiers, Saint-Aubin 91190, France
[e] Forschungszentrum Jülich GmbH, Institut für Energie- und Klimaforschung – Plasmaphysik, Jülich 52425, Germany

ARTICLE INFO

Keywords:
Tungsten
Metal-matrix composites
Fracture toughness
Snchrotron tomography
In-situ bending test

ABSTRACT

Due to a unique property combination, tungsten is a promising candidate for highly loaded areas in advanced fusion reactors. However, tungsten suffers from its inherent brittleness at low temperature and its susceptibility to operational embrittlement. In tungsten fibre-reinforced tungsten composites (W_f/W) the toughness is enhanced by extrinsic mechanisms of energy dissipation allowing toughening in the absence of any plasticity. In the here presented work active extrinsic mechanisms of toughening were shown on a model system for as-fabricated and embrittled samples. The mechanisms were evaluated by means of mechanical bending tests in combination with high energy synchrotron tomography. For that a novel 4-point bending test for the in-situ use with high energy synchrotron tomography was developed. Despite the high X-ray attenuation in tungsten a sufficiently high resolution was achieved and clear images of crack extension and crack-fibre interaction were obtained. Several active toughening mechanisms were observed and quantified for the as-fabricated state and, in the case of a stable fibre-matrix interface, also in the embrittled state. The toughening contribution of the individual mechanism was estimated using the mechanical test results and compared with analytically derived values. Using the determined values a high toughening was estimated for as-fabricated and for embrittled bulk W_f/W. The results give hope that the composite material will retain toughness even if experiencing operational embrittlement when used in a future fusion reactor.

1. Introduction

Tungsten (W) is the main candidate for highly loaded areas in advanced fusion reactors due to its excellent erosion resistance and low H retention as well as high temperature strength and creep resistance combined with a high thermal conductivity and melting point [1,2]. However, as a typical bcc metal, tungsten exhibits a so called ductile-to-brittle transition (DBT) [3]. Below a certain temperature, the DBT temperature (DBTT), these materials show brittle behaviour. In the case of tungsten the transition takes place well above room temperature and therefore strongly restricts its use. The transition temperature is very much dependent on the composition, the fabrication process, and the pre-treatment and is typically between 500 K and 600 K [4] and up to 1200 K for material annealed at high temperature [5].

Microstructure and toughness are strongly related in tungsten. For example highly deformed tungsten, e.g. tungsten wire, shows ductility even at room temperature [6,7]. This phenomenon makes tungsten prone to embrittlement by a change of microstructure for example during thermal overload in operation [8]. In the case of fusion operational embrittlement induced by neutron irradiation is an even larger concern [9,10]. Reviews about possible solutions and unsolved problems are given by Rieth et al. [11] and Wurster et al. [12].

In brittle materials like tungsten (below the DBTT) or ceramics stress cannot be redistributed. Areas with large local strain experience high stress levels and are therefore prone to brittle fracture [13]. The only way to improve the toughness in brittle materials is by *extrinsic mechanisms* [14,15]. Mechanisms like crack bridging, crack deflection or fibre pull-out dissipate energy and relax local stress peaks. Such purely mechanical mechanisms which work without the need of any plasticity are widely used in ceramic fibre-reinforced ceramics [16,17].

* Corresponding author.
E-mail address: johann.riesch@ipp.mpg.de (J. Riesch).

https://doi.org/10.1016/j.nme.2018.03.007
Received 13 December 2017; Received in revised form 11 March 2018; Accepted 12 March 2018
Available online 27 April 2018

Fibre pull-out is in general seen as the most effective mechanism [18,19]. Starting with Aveston et al. [20] extensive theoretical studies have been performed to describe these mechanisms of toughening. Detailed overviews are given by Evans [18] and Steinbrech [21].

Using such energy dissipation mechanisms to solve the brittleness problem of tungsten was suggested by several authors [22,23]. Extrinsic mechanism of toughening are introduced by reinforcing tungsten with tungsten fibres made of drawn tungsten wire. These fibres are coated by engineered interfaces in order to optimise their behaviour within the composite [24]. More information about these tungsten fibre-reinforced tungsten composites (W_f/W) can be found elsewhere [25,26]. The plastic deformation of the tungsten fibre was shown to be an additional effective mechanism of energy dissipation in W_f/W [27]. As the toughening is achieved by mechanical mechanisms it works in the as-fabricated state having a ductile fibre as well as in a state were the fibre has been embrittled. This was shown for bulk materials in [28,29] and gives hope to mitigate the problem of embrittlement during operation. Tungsten wire has been used in the past as reinforcements in copper composites [30], superalloys [31] and in a plasma sprayed tungsten matrix by Hill and Banta [32]. The main objective of these applications was however to increase the strength and creep resistance but not primarily the toughness.

In this article we investigate the active toughening mechanisms in the as-fabricated and in an embrittled state of W_f/W in detail. We do this on single-fibre composite model systems consisting of a single fibre surrounded by a tungsten matrix. As chemically deposited tungsten used as matrix material is already very brittle [33] the fibres were embrittled to study the embrittled state. The ductility and high strength in the tungsten wire used as fibres is due to its special microstructure. A heat treatment above the recrystallization temperature changes this microstructure by recrystallization and grain growth and embrittles the fibres as it was shown for the here used fibres in [7]. As similarly high temperature treatment of bulk tungsten typically leads to embrittlement [8], it was expected that the brittle behaviour of the matrix materiel should be preserved. Thus, a composite consisting of fully brittle constituents is created. This state is called embrittled W_f/W in the following.

To assess the toughening mechanisms in both cases it is essential that the macroscopic mechanical behaviour can be related to microstructural effects. As these effects are active during the fracture process (e.g. fibre bridging) their characterisation requires in-situ techniques. Mechanical testing in combination with tomography is well suited to assess the interaction of a growing crack with the microstructure and thus allows studying these effects. Synchrotron tomography allows to do this with a spatial resolution in the range of a few microns [34]. This was intensively used to study SiC fibre-reinforced Ti matrix composites (SiC_f/Ti) [35–38]. Quasi static as well as cyclic tensile tests have been used to evaluate the interaction between the fibres and the matrix in general and under loading at room temperature or at elevated temperature. Due to the very strong X-ray attenuation of tungsten, high energy synchrotron radiation is necessary to perform tomography experiments in this material. The high energy beamline ID 15A at the European Synchrotron Radiation Facility (ESRF) allows fast tomography and beam energies up to 500 keV and was therefore used in this work.

The same beamline was used for studying the tensile behaviour of similar model systems of W_f/W [27]. Despite the high X-ray attenuation in tungsten, a resolution of 5 μm was achieved and clear images of crack extension and deformation were obtained. The crack bridging and ongoing plastic deformation were directly observed in tomographic observations and correlated to the load-displacement measurements. The amount of absorbed energy due to plastic deformation of the tungsten fibre was determined and compared with values obtained from single-fibre tensile tests. Based on this work we present in the following the results of an experimental campaign of bending tests monitored by in-situ high energy tomography based on these experiences. Bending tests are used as they allow to grow a crack in a more controlled way than tension tests. The as-fabricated and the heat treated and thus embrittled state are compared. Emphasis is given on the expected transition of plastic bridging to purely elastic bridging as a consequence of the loss of fibre ductility. A weak interface consisting of a porous tungsten layer and a very stable interface consisting of an Er_2O_3 layer are investigated to determine the influence of the interface system on the toughening.

2. Extrinsic toughening by reinforcements

The matrix in W_f/W produced by chemical vapour deposition behaves brittle and thus linear elastic fracture mechanics are applicable [26]. An energy approach using the energy release rate G or the stress state at the crack tip characterized by the stress intensity factor K can be used. For linear elastic materials the two parameters are related as follows [39]:

$$K = \sqrt{G \cdot E^*} \tag{1}$$

where $E^* = E$ for plain stress conditions and $E^* = E/(1-\nu^2)$ for plain strain conditions (E: Young's modulus; ν: Poisson's ratio). The resistance of a material against fracture and thus its toughness is described by a critical value G_c or K_c, respectively [39]. For materials featuring extrinsic toughening the following equation is used:

$$G_c = G_0 + \Delta G$$

where G_0 is the toughness of the matrix material and ΔG the gain in toughness due to the extrinsic mechanisms. In the case of fibre reinforced composites, this gain can be described by the traction t caused by the fibres on the crack faces withstanding the crack opening u [18]. The following equation describes the contribution of the fibres ΔG_f to the toughness:

$$\Delta G_f = V_f \cdot w_f^* = V_f \int_0^{u_{max}} t(u)\mathrm{d}u \tag{2}$$

with

V_f	: fibre volume fraction	[-]
w_f^*	: specific energy consumption	[J m^{-2}]
u_{max}	: maximum crack opening	[m]
$t(u)$	: traction of reinforcements on crack faces	[MPa]

Based on this relationship, Becher [40] gives an overview about toughening mechanisms in ceramic fibre-reinforced ceramics. He describes two main contributions, crack bridging by intact fibres $\Delta G_{f,\,br}$ and pull-out bridging $\Delta G_{f,\,po}$ (typically also referred to as pull-out only). He describes bridging as a consequence of a force equilibrium and expecting a frictional component, respectively. In the absence of a frictional component the contribution to the toughness is calculated as follows:

$$\Delta G_{f,br,eq} = \frac{V_{f,br} \cdot (\sigma_{f,fr})^2 u_{db}}{2E_f} = V_{f,br} \cdot w_{br,eq}^* \tag{3}$$

with

$V_{f,br}$	: fibre volume fraction bridging crack plane	[-]
$\sigma_{f,fr}$	: fibre fracture strength	[MPa]
u_{db}	: debonding length	[m]
E_f	: Young's modulus of the fibres	[MPa m^{-2}]
w_{br}^*	: specific work by bridging	[J m^{-2}]

with a frictional component as follows:

$$\Delta G_{f,br,fr} = \frac{V_{f,br}\, r}{3E_f \tau_i} (\sigma_{f,fr})^3 = V_{f,br} \cdot w_{br,fr}^* \tag{4}$$

with

r	: fibre radius	[m]
τ_i	: frictional shear resistance	[MPa]

In contrast to Becher et al. we use a factor of 3 instead of 6 (see

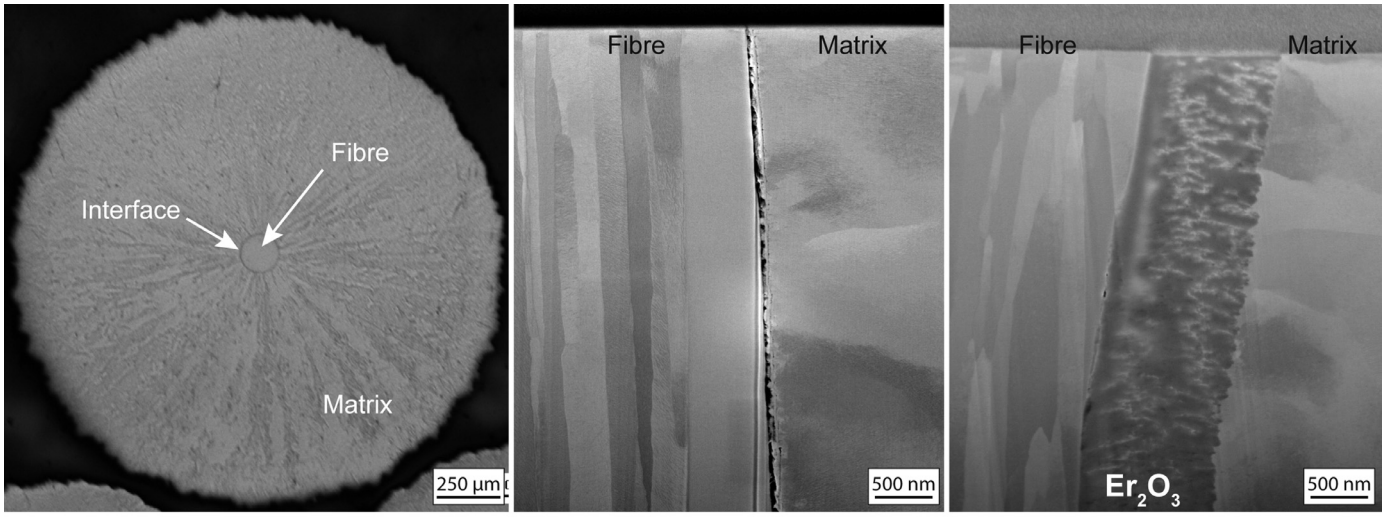

Fig. 1. Scanning electron microscopy (SEM) pictures of the cross section of (a) a single fibre composite and (b) and (c) longitudinal sections showing the interface region for the different interface types in detail. Picture (b) shows a porous interface region caused by a partial decomposition of the WO_x interface during the matrix production. In (c) the dense Er_2O_3 interface layer is clearly visible.

Appendix A for details).

The contribution of pull-out bridging to the toughness ΔG_{po} can be approximated by assuming a constant shear stress τ resisting the fibre sliding [18]. Using Eq. (2) and the function $t(u) = \tau 2r\pi(h-u)$ which describes the energy consumption along the pull-out length h, $\Delta G_{f,\,po}$ is calculated in relation to the frictional shear strength τ as follows:

$$\Delta G_{f,po} = V_{f,po} \cdot w^*_{po} = V_f \cdot \frac{\tau 2 {h_{max}}^2}{r_f} \tag{5}$$

with

$V_{f,po}$	: fibre volume fraction being pulled out	[-]
w^*_{po}	: specific work by pull-out	[J m^{-2}]
τ	: frictional shear stress	[MPa]
h_{max}	: final pull-out length	[m]

In W_f/W a very prominent third mechanism is the plastic deformation of the individual fibres. The contribution of this mechanism to the toughness $\Delta G_{f,\,pl}$ was estimated by Riesch et al. [27]. It can either be calculated using the stress distribution in the reinforcements $\sigma(u)$ for the traction $t(u)$ in Eq. (2) or by using an analytical relationship first presented by Ashby et al. [41] and used in [27] for W_f/W.

The tomographic observation was used to identify active toughening mechanism and the specific energy consumption by the respective mechanism was evaluated using the measured load displacement behaviour related to the cross-section of the fibre. The measured data was compared to theoretical approaches using Ashby's relation for the ductile case and Becher's relations for the elastic/brittle case. The input to these equations was either extracted from the actual experiment or by using earlier investigations of W_f/W. As this was done for different as-fabricated and embrittled samples the measurements allowed to get insight into the effectiveness of the different toughening mechanisms at various states of W_f/W. For this the obtained data was related to bulk material with a fibre volume fraction of 0.3.

3. Experimental

3.1. Specimen preparation

Samples containing a single fibre so called single fibre composites (SFC) were chosen as a model system. The samples consist of a coated single tungsten fibre embedded in a tungsten matrix which is produced by chemical vapour deposition (CVD). In these systems, the mechanical behaviour automatically reflects the influence of a single fibre. This allows a clear and simple correlation of microscopic effects, e.g. toughening mechanisms, with the macroscopic stress-strain behaviour. Consequently such samples are intensively used to investigate interface properties in composites in general [16,42] and have been used in synchrotron studies to investigate SiC_f/Ti composite systems [35,43]. SFCs have also been used in high energy synchrotron tomography studies of W_f/W [27].

The tungsten fibre is made of commercial tungsten wire (K Draht Typ B) with a diameter of 150 µm which is provided by the OSRAM GmbH, Schwabmünchen. Because of its unique microstructure the drawn wire exhibits a high strength of more than 2900 MPa and ductility even at room temperature with a failure strain larger than 2%. A detailed description of the wire is given in [7].

The interface coating was fabricated by means of magnetron sputtering. Two different coatings were investigated: 670 nm of WO_x and 1000 nm of Er_2O_3. Er_2O_3 was chosen due to its high temperature stability. WO_x was chosen as representative of a weak interface as it is not stable during the matrix production process and forms a porous interlayer (see Fig. 1(b)). The Er_2O_3 coating was produced in a bi pulsed mode using two cathodes with 300 W each and a frequency of 75 Hz. 160 sccm[1] Ar and 10 sccm O_2 are used as deposition process atmosphere. The WO_x layer is produced using 300 W RF power with a tungsten target. 10 sccm Ar and 10 sccm O_2 are used to form the oxide layer. In this case a protective tungsten layer with a thickness of 80 nm was deposited afterwards. Details of the interface deposition process are given by Du [22, p. 43 ff].

The tungsten matrix was deposited by a chemical vapour deposition (CVD) process. Gaseous WF_6 is reduced by H_2 in a heterogeneous reaction at the fibre surface. Beside a solid W deposit gaseous HF is formed as a by-product. The deposition temperature was 830 K with a processing time of 30 h. Zinn [44] describes the CVD process of W in detail. The final specimens had a diameter ranging between 1.5 and 2 mm. Due to the moderate processing temperature and the force less character of the chemical deposition process the microstructure of the fibre is preserved during the matrix deposition process (see Fig. 1(c)). Due to the benign processing and as fibre and matrix have similar

[1] Standard cubic centimetre per minute.

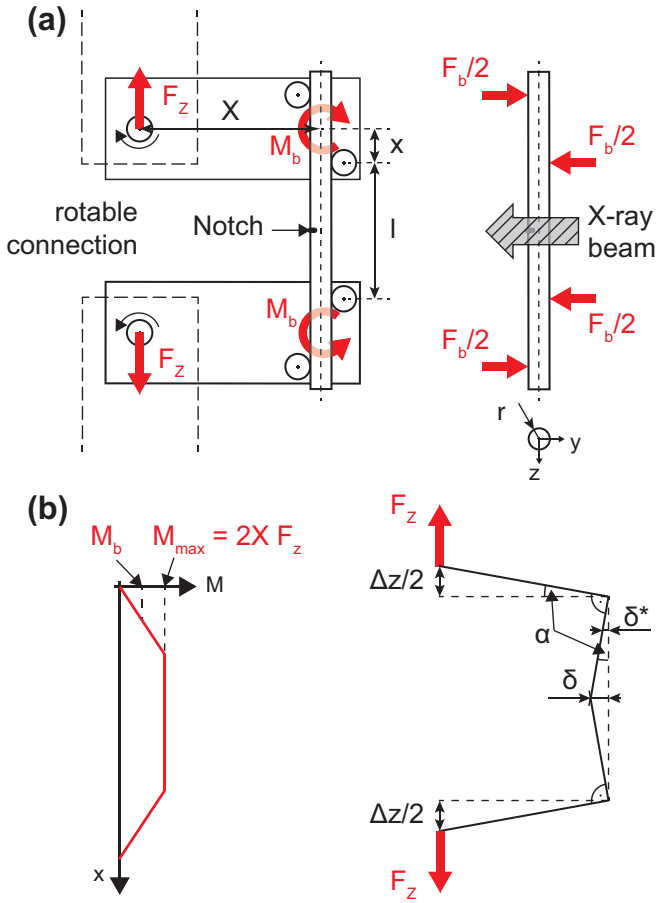

Fig. 2. Schematic drawing of an upright 4-point bending test. In (a) the force relations alternating a tension force into a bending force are shown. In (b) the corresponding momenta (left) and the relation for the determination of the deflection (right) are given.

properties the residual stress in W_f/W is expected to be low. A detailed discussion about this topic is given in [27].

In Fig. 1 metallographic sections of the specimen are shown. Fig. 1(a) shows a cross-section with the coated fibre in the centre surrounded by the matrix having a star like structure of columnar grains. In (b) and (c) the fibre-matrix-interface region is shown in detail in a longitudinal section. Fig. 1(b) shows the WO_x interface which has been strongly affected by the matrix production process. The interface between fibre and matrix consists of porous area rather than a dense layer. Fig. 1(c) shows the sample with the Er_2O_3 interface which is clearly visible. In both cases, the matrix features a more isotropic grain structure and the fibre is strongly textured with elongated grains.

To maximize the specimen volume for a given maximum penetration depth of the synchrotron radiation, a cylindrical sample geometry is chosen. The same process as described in [27] was used to achieve a final diameter in the measuring area of 1 mm and a sharp, 4 μm wide and 40 μm deep, pre-crack at the root of a 80 μm wide and 100 μm deep notch. Specimens in the as-fabricated and in an embrittled state were tested. As described above a heat treatment was carried out at 2000 K for 30 min to embrittle the samples. The heat treatment was done similar as described in [45].

3.2. Tomography

Due to the strong attenuation of X-rays in tungsten based materials high X-ray energies are needed to achieve a sufficient penetration depth. Therefore the high energy beamline ID15-A at the European Synchrotron Radiation Facility (ESRF) in Grenoble was used for this investigation. Methods established at previous experiments on tungsten based materials [27,46] were improved and combined with a bending test capability. The optimum sample thickness is a compromise between requirements for tomography and for the mechanical test. This problem is discussed in detail elsewhere [27]. In this study a sample thickness of 1 mm was defined as the compromise between testing volume, tomographic resolution and duration of measurement.

We used white beam in the energy range of 60–240 keV. 600 projections with an exposure time of 300 ms each over a rotation angle of 180° were collected for one tomogram (total acquisition time 3 min). As scintillator a LuAG:Ce (Screen) with a thickness of 25 μm was used. A 10x mirror objective and a Frelon 2k camera (2048 × 2048 px, pixel size 1.4 μm) were used to record a picture. With that system setup the spatial resolution was improved to 3–4 μm compared to 5 μm in previous experiments. Similar to the previous experiments a special aperture–in this case made of silver–was used to avoid premature camera saturation on the peripheral domains of the samples (details in [27]). In addition 40 mm of Si and 7 cm of water were placed in front of the sample to regulate the beam energy. The 3D microstructure of the sample was reconstructed from the 2D projection images using a standard filtered back-projection algorithm [47] and the software ImageJ/Fiji [48] was used for image analysis.

3.3. Bending test

For the in-situ bending a mechanical testing machine specially designed to be used together with synchrotron tomography was used in combination with newly designed bending equipment. Details of this equipment are explained in the next paragraph. The machine has been used for tension tests on single-fibre W_f/W samples [27] and a detailed description can be found elsewhere [49]. The maximum load is 5 kN with a minimum displacement rate of 0.1 $\mu m\,s^{-1}$. The load was measured by a 500 N range load cell and the displacement was calculated using the displacement of the machine's upper grip. The bending test was performed step wise in a displacement controlled mode. A tomogram was taken at each bending increment.

3.3.1. Upright 4-point bending test

An upright 4-point bending test setup moving the force transmission points out of the measuring area and allowing the transmission by the synchrotron beam was designed. In Fig. 2 the basic idea of the setup is shown schematically. Specially designed specimen holders are used to alternate the direction of the force transmission into a vertical position. They consist of a mounting system attached to a rotatable lever arm. As these arms are rotatable only a bending moment is generated if the mounting system moves apart. Two pins at the end of these arms allow the mounting of the sample. By applying a tensile load, the lever arms move apart and tilt applying a bending force on the specimen. Using the geometrical relations of the setup the tension load and the displacement can be transferred to the corresponding bending load and deflection values. A detailed explanation is given in Appendix B.

4. Results

In total 8 out of 21 prepared samples have been tested successfully during the tomographic campaign. The results summarized in Table 1 are presented in detail in the following paragraph.

Fig. 3 shows representative load displacement curves for as-fabricated (a)/(b) and heat treated (c)/(d) samples for both tested interfaces. The load is given as bending load F_b calculated using Eq. (B.1). The displacement is given as deflection of the inner force transmission points δ^* calculated using Eq. (B.3). Due to problems in the data acquisition system some parts of the curves are only shown qualitatively (dotted lines).

Two samples in as-fabricated case showed at first a linearly

Table 1
Overview of bending results.

	Treatment	Interface	F_b (matrix failure) [N]	σ_n (matrix failure) [N mm^{-2}]	F_b (fibre straining) [N]	u [μm]	A_{red} [μm^2]	φ [°]	h_{max} [μm]
1	as-fabr.	Er_2O_3	33	45	15	97 ± 3	11.1×10^3	10	
2	as-fabr.	Er_2O_3	n. a.	n. a.	11	88 ± 3	10×10^3	11	
3	as-fabr.	Er_2O_3	n. a.	n. a.	12	(63 ± 3)	(14.3×10^3)	10	
4	as-fabr.	WO_x	29	49	13	80 ± 3	11.2×10^3	11	
5	embrittled	Er_2O_3	17	29	10	2.0 ± 6			n. a.
6	embrittled	Er_2O_3	53	103	n. a.	n. a.			n. a.
7	embrittled	Er_2O_3	23	35	10	2.0 ± 6			75
8	embrittled	WO_x	34	68	n. a.	n. a.			n. a.

n.a. not applicable.

increasing load. After reaching a maximum, a sharp load drop occurs. This is followed by a region with approximately constant load (see Fig. 3(b)). For two samples this linear increase is missing and the curve behaves concave before reaching a plateau with constant load at a similar load level (see Fig. 3(a)). In both cases a second load drop occurs at which the sample does not fail completely but cannot anymore bear load. In the case of the heat treated samples all samples show at first a linear increase in load followed by sharp load drop. In the case of the Er_2O_3 interface an intermediate regime is observed for two samples. Following the first load drop, the load increases again before a second drop occurs (see Fig. 3(c)). One sample with Er_2O_3 interface as well as the sample with WO_x interface shows a load drop to a very low value where it stays constant with ongoing displacement (see 3 (d)). The load level is comparable to the final load of the Er_2O_3-samples. No further load drop is detected in this case. For the shown heat treated samples bending of the specimen went on over a large displacement range with

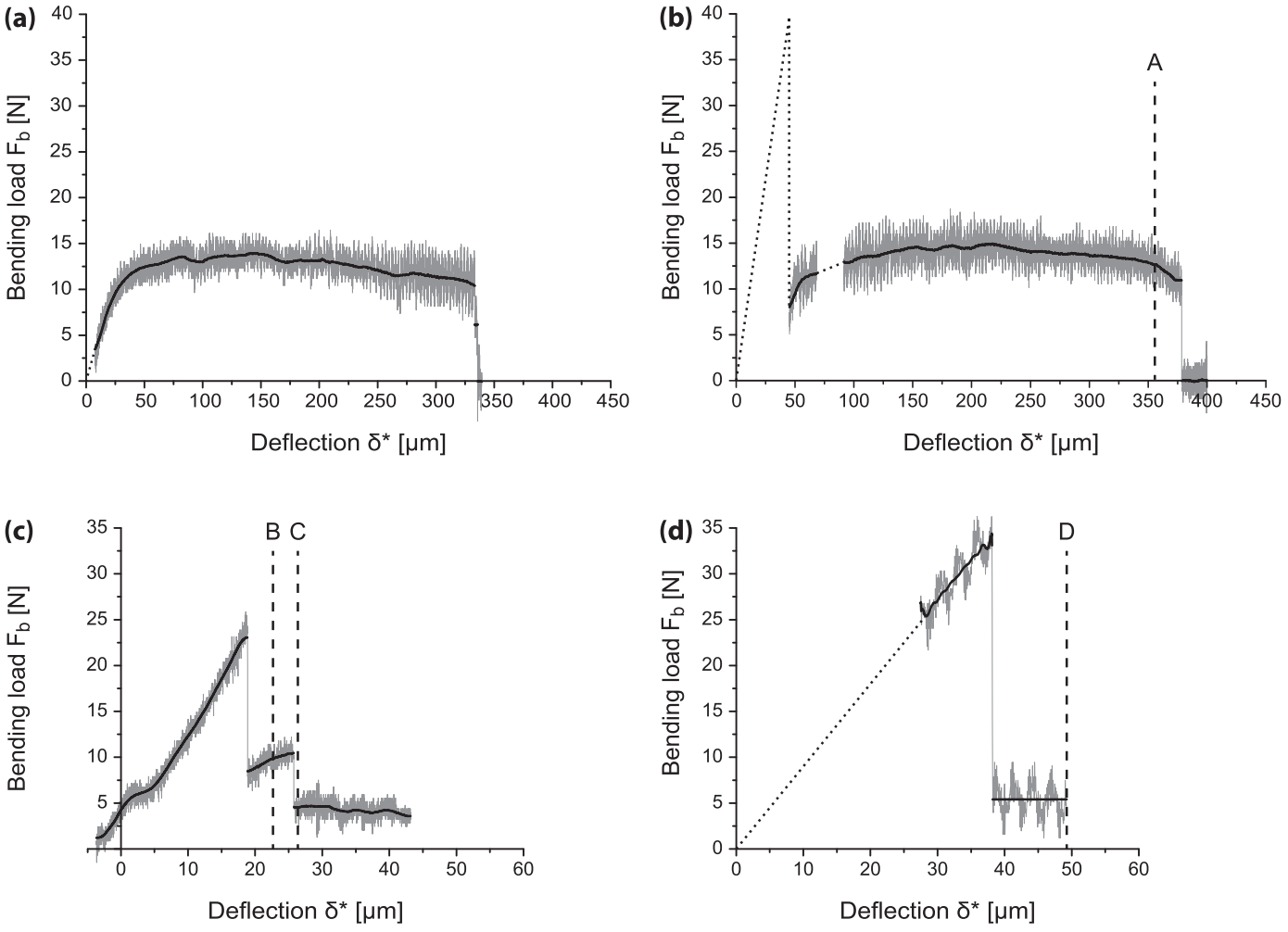

Fig. 3. Representative force-displacement curves for bending test on (a)/(b) as-fabricated and (c)/(d) heat treated samples. Curves for two different interface types are shown: (a)/(c) Er_2O_3 and (b)/(d) WO_x. The curves are extracted from a force–time measurement using the displacement rate of the testing machine. The measured load signal showed a strong oscillation (light grey curve) caused by the motor of the machine. The full lines represent the smoothed data curves (weighted average). According to the numbering in Table 1, curve (a) shows sample 1, (b) sample 4, (c) sample 7 and (d) sample 8. The vertical dashed lines indicate the displacement levels at which a tomographic measurement shown later in this article was performed. The bent in the loading of curve (c) was caused by the setting of the system.

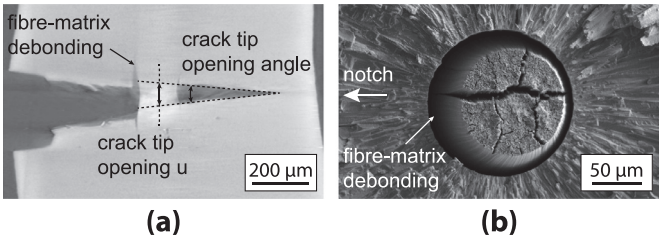

Fig. 4. (a) Last available tomographic reconstruction before the fibre fails and (b) SEM image of the fracture surface for a sample with WO_x interface (sample 4 in Table 1). The load displacement curve of this sample is shown Fig. 3(b) in which the displacement level of the tomogram is indicated by label A. Fibre-matrix debonding is visible both in the tomogram and in the SEM image. In (b) the side where the artificial notch is located is indicated by a white arrow.

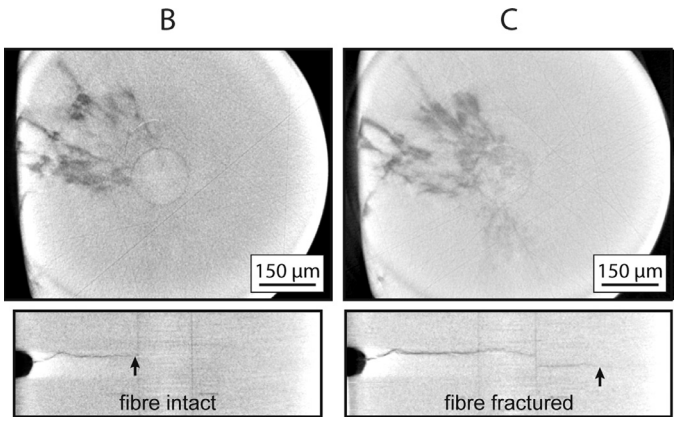

Fig. 5. Tomographic sections at specific displacement levels for a sample with an interface of Er_2O_3 showing an intermediate load regime. Crack bridging is shown in cross-sections through the crack plane (upper row) and longitudinal sections through the fibre centre (lower row). The corresponding displacement levels are indicated in Fig. 3(c). The black arrows indicate the crack tip.

almost no measurable load before final failure (not shown in the figure).

The tomographic observations allowed a more detailed understanding of the material behaviour and active effects. In the as-fabricated state the first load drop corresponds to the crack initiation in the matrix for the samples showing a linear loading. The fibre stays intact and bridges the crack. For the other samples matrix fracture was detected already in the unloaded state probably happened during mounting. Also in this case the fibre was intact bridging the crack. In all cases, the crack opened and the fibre was strained with on-going bending. After a large plastic deformation including necking, the fibre finally fractured. The plastic deformation of the fibre has been observed in several reconstructed volumes for all as-fabricated samples. The crack tip opening and thus the elongation of the fibre as well as the opening angle were measured using the last tomographic observation before the fibre fails (see Fig. 4(a)). Two lines are fitted on the crack flanks and the crack opening respectively the elongation of the fibre is measured using a line integral at the centre of the fibre. The angle between the lines gives the crack tip opening angle. The location of this tomographic observation on the bending curve is indicated in Fig. 3(b) label A. As a measure of the plastic deformation the reduced cross-section of the fibre at this displacement level was determined by fitting an ellipse in the tomographic cross-section. In Fig. 4(b) the fracture surface of such a sample is shown. The strong plastic deformation is well visible as elongation and necking. It is important to note that due to the large deflection significant bending occurs. As a consequence unsymmetrical debonding is observed however the necking looks still very symmetric (see Fig. 4(b)). The matrix shows a mixture of cleavage and grain boundary failure.

Bridging was also observed in the heat treated samples with ErO_x interface. In these samples the fibre stays intact after crack initiation has occurred in the matrix. With ongoing displacement the fibre was strained elastically and finally fractured. No obvious deformation was observed in the fibre. In Fig. 5(a) this behaviour is illustrated by tomographic sections at two displacement levels which are also indicated in Fig. 3(c). At level I (label B) the fibre is intact and bridges the crack. At level II (label C), shortly after the second load drop, the fibre has failed.

In addition the tomographic observations revealed fibre pull-out in one Er_2O_3 sample. Fig. 6 shows a tomographic reconstruction for this sample at which the crack plane of matrix and fibre were located in different heights. Thus with ongoing displacement the fibre was pulled out of the matrix. Based on the tomographic observation the pull-out length h_{max} for this sample was determined to be 75 µm. It has to be noted that this sample did not show the intermediate load plateau as other samples with Er_2O_3 interface.

The tomographic observations of the sample with a WOx interface showed that the first and only load drop (see Fig. 3(d) label D) was accompanied by the failure of the fibre. The tomogram shown in Fig. 7 has been obtained shortly after the load drop (displacement level is indicated in Fig. 3(d)) and reveals that the crack had propagated through the fibre and almost through the whole sample.

In Fig. 8 representative fracture surfaces of the heat treated samples are shown. For the sample with Er_2O_3 interface the fibre and matrix are clearly distinguishable (a,b). On a larger magnification picture the Er_2O_3 interface is clearly visible (c). For the WO_x interface sample no clear interface between fibre and matrix is visible (d,e). Even on a larger magnification the WO_x cannot be observed (f). In general the fibre fractured with a mixture of cleavage and intergranular fracture. The fracture planes of fibre and matrix are different for the Er_2O_3 sample and they coincide for the WO_x sample. The matrix fractured similar to the as-fabricated state (see Fig. 4(b)) in a mixture of cleavage and grain boundary failure.

In Table 1 the measured values for the as-fabricated and embrittled samples are summarized. The bending force F_b and the nominal stress – disregarding the stress concentration – at the notch using Eq. (B.2) are given at the initiation of matrix failure. These values are missing for sample 2 and 3 as these were fractured during mounting. For those samples the nominal elastic stress at crack initiation in the matrix is missing. Beside sample 6 all samples showed very similar results. The crack initiation took place in a load range of 17–34 N corresponding to a stress between 29 and 68 N mm^{-2}. Sample 6 showed significantly higher load and stress. For samples where the fibre stays intact during matrix cracking the mean bending force for fibre straining was very similar for all cases and lies between 10 and 15 N. The deflection δ^* is different for both interfaces due to different sample geometries and is therefore not given in the table. However two main observations are made: in general, the deflection at crack initiation in the matrix was comparable for the as-fabricated and embrittled case and the deflection at which the fibre fractures was ten times larger in the as-fabricated case.

The crack opening u was determined using the last available tomographic reconstructions before fibre fracture. This means depending on the location of the tomogram that the crack opening is underestimated. This is the case for sample 3 where the tomogram was taken far before fibre fracture and thus crack opening and reduced area are much smaller. For the other as-fabricated samples u was around 90 µm for both interface types compared to a very small opening of 2 µm in the embrittled case. Due to this small opening the crack tip opening angle φ is only given for the as-fabricated samples. For this case, the reduced area A_{red} caused by the ductile deformation of the fibre is given in addition. It was comparable for both interfaces. As pull-out was not observed in the as-fabricated case and only for sample 7 in the embrittled case the pull-out length h_{max} is only given for that sample.

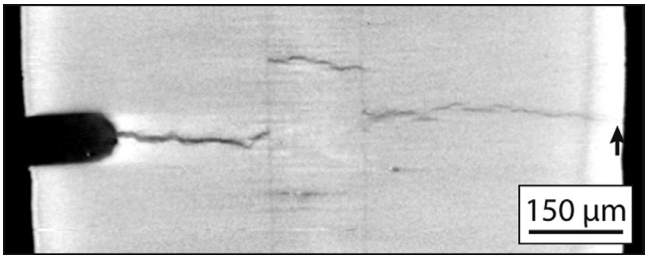

Fig. 6. Longitudinal section of a tomographic reconstruction for a sample which features different crack planes for the fibre and the matrix. The section was taken of the first tomogram taken after crack initiation. The black arrow indicates the crack tip.

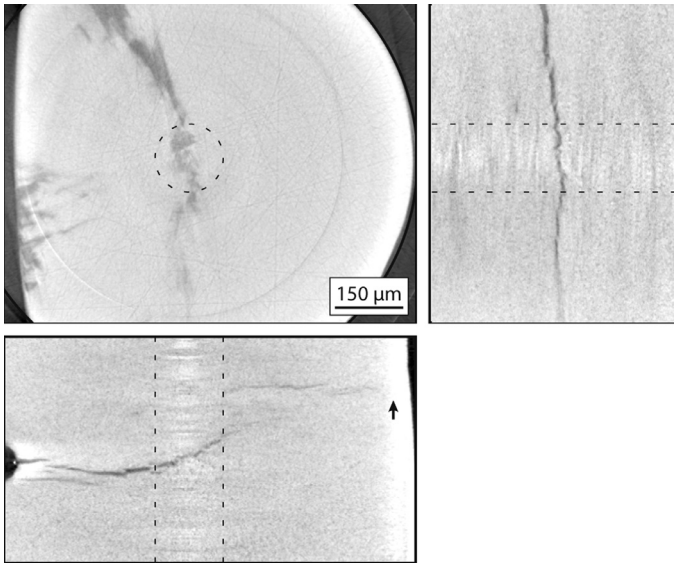

Fig. 7. Tomographic sections of the heat treated sample with an WO_x-interface. Cross-sections through the crack plane and longitudinal sections through the fibre centre viewed from two directions are shown. The state after the load drop (compare Fig. 3(d)) is given. The crack has propagated through the fibre. The black arrow indicates the crack tip. The position of the fibre is indicated by dotted lines.

5. Discussion and quantitative assessment of toughening effect

A limited number of samples has been tested due to time constraints and complexity of high energy tomography. This is taken into account for the discussion of the results. Ex-situ experiments will be used to confirm the findings.

Compared to tension tests the here used bending tests allow for an easier achievement of stable crack propagation as under bending load the stress decreases along the cross section. The following equation allows an easy estimation of the maximum sample size allowing an embrittled fibre to survive a matrix crack in a tension test (assuming full load transfer to the fibre) [50]:

$$r_{ges} \leq r_f \sqrt{\frac{\sigma_{f,u}}{\sigma_{m,u}}} = 220\,\mu m \tag{6}$$

with

r_{ges}	: maximum sample radius	[µm]
r_f	: fibre radius	[150 µm]
$\sigma_{f,u}$	: fibre strength, embrittled	[900 ± 30 MPa] [7]
$\sigma_{m,u}$	: matrix strength	[420 MPa] [27]

With the used sample geometry it would not have been possible for the fibre to survive the crack initiation in the matrix in a tension test. The decrease of sample size to the required amount is not reasonable as the matrix should be much larger than the fibre to allow for notching and for the observation of the bypass of the crack around the fibre. However, bending tests lead to a more complex loading situation e.g. large bending (see Fig. 4) and thus a more complex stress distribution not necessarily reflecting the actual situation in a real structure. As the effect increases with increasing bending deflection the as-fabricated state is affected more significantly whereas in the embrittled state the effect is expected to be low.

As expected the brittle nature of the CVD-W used as matrix material was preserved during the heat treatment. The load-displacement behaviour up to crack initiation in the matrix as well as the fracture surfaces (compare Fig. 4(b) with Fig. 8(c) and (f)) look very similar for both states and show typical brittle behaviour. The loads and the deflection needed for crack initiation are very similar for as-fabricated and embrittled samples (see Table 1). In fact the spread in-between the embrittled samples was higher than the difference between the two states. This means that the cracking resistance and thus the toughness of

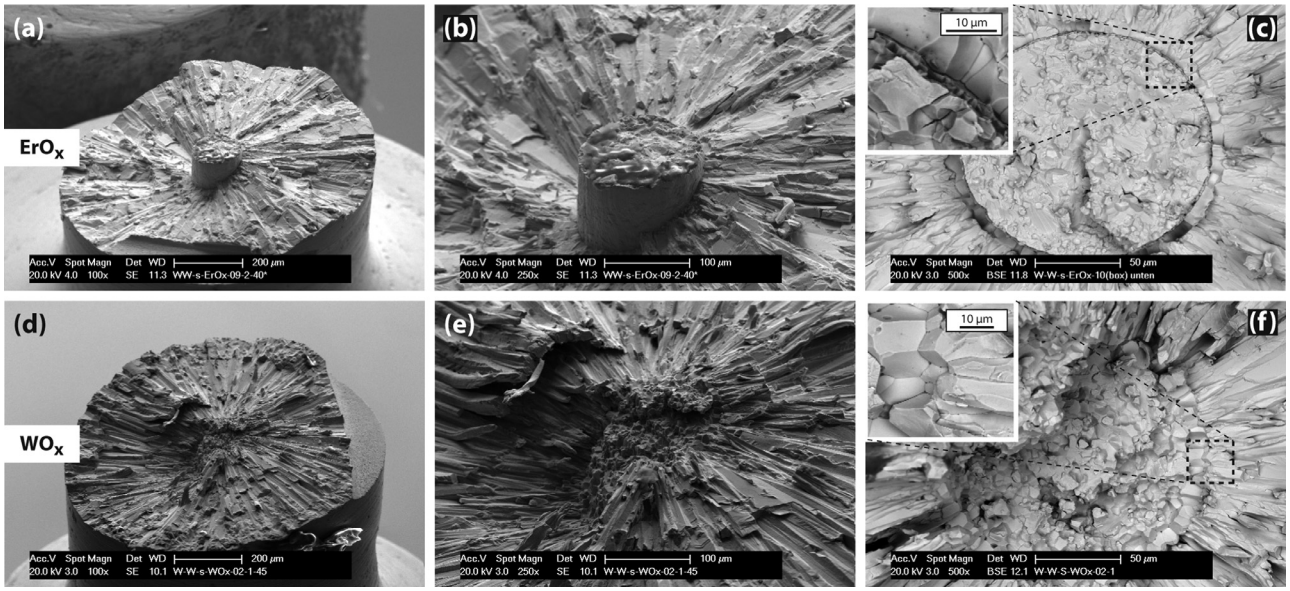

Fig. 8. SEM pictures of the fracture plains of heat treated samples having an ErO_x-interface (picture (a)–(c)) and a WO_x-interface (picture (d)–(f)), respectively. In (a) and (d) an overview is given. In (b) and (e) the fibre is shown in detail. (c) and (f) show the fibre fracture surface in an overview and the interface region in detail.

Table 2
Overview on energy dissipation mechanisms.

	Treatment	Interface	$W_{f,\ pl}$ [mJ]	$w^*_{f,pl}$ [mJ mm^{-2}]	κ_w [-]	$W_{f,\ br}$ [mJ]	$w^*_{f,br}$ [mJ mm^{-2}]	$W_{f,\ po}$ [mJ]	$w^*_{f,po}$ [mJ mm^{-2}]
1	as-prod.	Er_2O_3	5.8	3.3×10^2	2.2	n .a.	n .a.	No pull-out in ductile case	
2	as-prod.	Er_2O_3	3.9	2.2×10^2	1.5	n .a.	n .a.		
3	as-prod.	Er_2O_3	n .a.	n .a.	n .a.	n .a.	n .a.		
4	as-prod.	WO_x	4.1	2.7×10^2	1.8	n .a.	n .a.		
5	embrittled	Er_2O_3	No plastic deformation in embrittled case			0.08 ± 2	4.4 ± 9	n .a.	n .a.
6	embrittled	Er_2O_3				n .a.	n .a.	0.17	9.6
7	embrittled	Er_2O_3				0.035	2	n .a.	n .a.
8	embrittled	WO_x				n .a.	n .a.	n .a.	n .a.

n.a. not applicable.

the matrix seems to have not been significantly changed. A similar behaviour was observed for pure matrix material [23] and for bulk composite material [28,29]. As brittle material does possess very little resistance against crack growth once it it is initiated, the growth is dominated by the composite structure and thus in our case mainly the fibre.

In the as-fabricated state all samples showed crack bridging by the fibre after crack initiation in the matrix followed by an intense plastic deformation of the fibre. After the matrix fractured the fibre was strained and thus contracted laterally and due to sufficiently weak interfaces fibre-matrix debonding occurred. With increasing load the contraction continued and necking occurred. The debonding as well as the necking is visible in Fig. 4(a). This behaviour was also observed during in-situ tomographic studies of tension tests on similar samples [27]. Finally the fibre fractures by fully ductile knife-edge necking of individual grains (see Fig. 4(b)). This fracture behaviour is typical for tungsten fibres [7,51,52] and was observed for W_f/W [27] where the crack opening and the area of reduction are very similar to the results obtained here. Necking of the fibre starts in the crack plane of the matrix. The fibre necks and thus fractures in the same plane as the matrix. As a consequence of the necking there is no contact between fibre and matrix at fibre fracture. Therefore, pull-out mechanism were not observed in the as-fabricated samples. In the as-fabricated case there is no significant difference in the behaviour of the samples having different interface systems.

The plastic deformation energy was calculated directly using the measured values and then compared with an analytical treatment based on the investigations by Ashby et al. [41]. The matrix has a brittle behaviour [33] and can therefore not consume significant energy after crack initiation. It is therefore assumed that the interaction of the crack with the fibre gives the main contribution to the energy consumption reflected in the load displacement curves. The following effects might occur: the debonding and frictional sliding of the fibre-matrix interface as well as the elastic and plastic deformation of the fibre. The interface effects occurred immediately after crack initiation and their overall contribution is therefore expected to be low. The elastic loading of the fibre is reflected by the linear regions in the load displacement curves after matrix cracking which are very small compared the whole curve. Therefore, the plastic deformation energy $W_{f,\ pl}$ was estimated by integrating the force-displacement curve after matrix fracture. The specific plastic deformation energy $w^*_{f,pl}$ per unit area is calculated by considering the actual dimension of the fibre: $w^*_{f,pl} = W_{f,pl}/r_f{}^2\pi$. In Table 2 the corresponding values are given for the different samples. It can be seen from those values that there is no significant difference between the two interface types. Obviously it has to be taken into account that due to the large crack opening significant bending occurs which possibly influences the deformation behaviour.

Another way of calculating the plastic deformation energy was proposed by Ashby et al. [41] and used before for W_f/W in tension tests [27]. Assuming a yield strength $\sigma_e = 2000$ MPa [7] the so called toughening parameters for the samples tested here are calculated and given in Table 2. In Fig. 9 they are shown in comparison to the tension test result by Riesch et al. and Ashby's tests results. The tension test result was recalculated with the higher yield strength value used here. Similar to results for the tension test the gradient of normalised energy over normalised displacement appears to be smaller than for Ashby's results but still within the same range. This shows that indeed the plastic deformation of the fibre plays the dominant role. Furthermore, these results support the theory of Riesch et al. that for W wire the relation between the normalised energy and the normalised crack

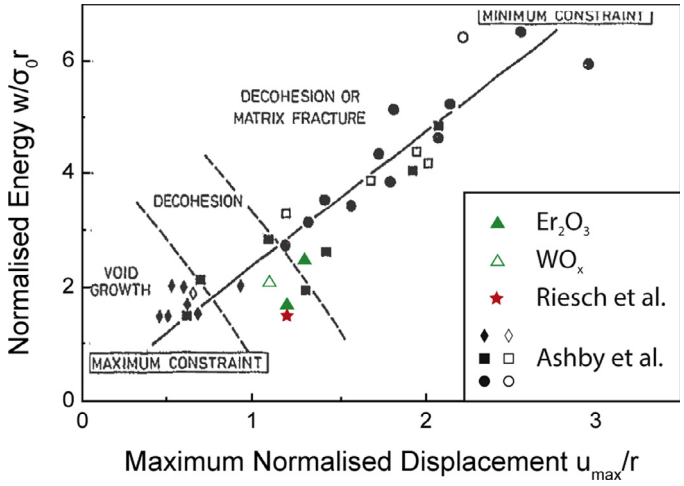

Fig. 9. Normalised energy over normalised crack opening for the as-fabricated samples in a diagram given by Ashby et al. [41] with the tension test result of W_f/W Riesch et al. [27].

opening follows a smaller gradient due to the lower possible strain hardening effect. Although the relations are derived for tension tests it is quite significant that they seem to be applicable for the here presented bending tests. The sample seems to somehow self align in a way that in the centre probably mainly tension load occurs (see Fig. 4(a)). This theory is backed by the fact that the here measured deformation energy is very similar to the one determined in the tension tests.

In the embrittled state the fibre fractured brittle in a mixture of grain boundary failure and cleavage. The fracture surfaces look very similar to results obtained in single fibre tests exposed to a heat treatment of 1900 K. As reported there the reason for this behaviour is most certainly the loss of the elongated fine grain structure. The interaction of the brittle fibre with the crack depends on the interface type. If the interface stays intact the embrittled samples also show crack bridging. This is the case for the samples with an Er_2O_3 interface. By combining the tomographic observations and the force-displacement measurements this bridging is clearly shown. With ongoing displacement/bending the fibre is strained until fracture. Due to a lower strength and a lack of ductility fracture strain is low which leads to a small crack opening.

A direct way to determine energy consumption is, as in the ductile case, to integrate the force displacement curve. As discussed in the ductile case the contribution of the matrix is considered to be low as well as the effect of frictional sliding and bending due to the very small crack opening. Neglecting the contribution by debonding the determined energy gives an estimation about the bridging energy. As in this case the fibre is brittle only elastic loading contributes. The calculation was possible for two samples resulting in a bridging energy of $w^*_{f,br} = 2 \times 10^{-3}\mathrm{J\,mm^{-2}}$ and $4.4 \pm 0.9 \times 10^{-3}\mathrm{J\,mm^{-2}}$, respectively. The result of the second sample was based only on the load measurement right after matrix fracture and the recorded overall displacement until fibre fracture due to problems in the data acquisition system. This leads to a large error and the value is therefore not used for the further calculations.

The very small extend of crack opening makes it very hard to be measured directly in the tomograms but nevertheless for some samples the crack was clearly visible. Assuming a crack opening $u_{rec} = 2.0 \pm 0.6$ µm (corresponding to 1–2 pixels) the stress state during bridging is further investigated. With a zero fibre load at crack initiation and $\sigma_{f,\,fr}$ at maximum crack opening u_{rec} as well as a linear elastic behaviour following relation is valid:

$$w^*_{f,br} = \frac{1}{2} u_{rec} \cdot \sigma_{f,rec}$$

and thus

$$\sigma_{f,rec} = \frac{2w^*_{f,br}}{u_{rec}} = 2000^{+860}_{-460} MPa \tag{7}$$

The large uncertainty is a result of the above mentioned uncertainty in the crack opening measurement. However the determined strength of the fibre seems very high compared to measured values in tension tests on single fibres of 900 ± 30 MPa [7]. These values are for free fibres without any constraint. A reason for the difference is probably the very short loading length in the constraint case. In brittle material fracture is promoted by defects. The smaller the volume, the smaller the probability of failure at a certain load. Such size effects are well known [53] and have been reported for fibres [54]. This high strength explains why the load needed for fibre straining is comparable to the as-fabricated case (see Table 1). It has to be mentioned that as the contrast between the matrix and the crack (in this case W and air) is huge the actual crack opening might be even smaller than the size of the corresponding pixels. A smaller crack opening would lead to a more comparable fibre strength as presented in [7] but would not explain the similarity in the load values.

The determined strength allows to calculate the fracture strain of the fibre $\epsilon_{f,\,fr}$ (linear elastic behaviour) and thus the corresponding debonding length u_{db}:

$$u_{db} = u_{max}/\epsilon_{f,fr} = 400 \pm 120\,\mu\mathrm{m} \tag{8}$$

This debonding length seems quite high. As this case is based, similar to Eq. (3) of Becher, on force equilibrium a frictional component might be active lowering the actual debonding length.

Assuming a frictional component according to Becher's considerations (see Eq. (4)) The frictional shear stress required for this case is:

$$\tau_i = \frac{r_f}{3E_w w^*_{f,br}} (\sigma_{f,rec})^3 = 250^{+480}_{-140} MPa \tag{9}$$

with

r_f 75 µm : fibre radius
E_w 400GPa : Young's Modulus tungsten

The cubic dependence of this equation on the fibre stress together with the large uncertainty of this value (compare Eq. (7)) leads to a large uncertainty in the determined shear stress. The determined shear stress is significantly higher than the values determined by Du [22] in push-out tests for a similar interface of 64 MPa. However frictional shear strengths up to 170 MPa have been observed for thinner Er_2O_3 interfaces (0.6 µm) in these investigations. Using the calculated value the debonding length is calculated to be $300^{+210}_{-150}\mu m$ which seems to be in the right range.

In summary the relations given by Becher seem to show the right trend but do not fully represent the real situation. Further investigations are needed to determine the actual situation of debonding and stress state as well as to adopt the analytical description accordingly. Very helpful would be a more precise determination of the crack opening and a measurement of the strength of brittle and constraint fibres.

After the heat treatment the fibre fractures in a brittle manner. In a brittle fracture the crack position is determined by local weakness or random flaws. Therefore, the crack position in fibre and matrix are not necessarily in the same plane. In that case frictional pull-out can contribute to the toughening. This was directly observed in the tomographic pictures of one test. The observed pull-out length was $h_{max} = 75$ µm. For being pulled out the fibre needs to be debonded first. Pull-out length might be smaller than debonding length as the matrix fracture plane might cut the fibre within the debonded region and not necessarily at its very end. This could explain why the obtained value is much smaller than the values obtained for the debonding during elastic bridging. Another reason could be a lower fracture strength of the fibre leading to a lower debonding length (see Eq. (8)) and thus a lower possible pull-out length. Such a strength variation is realistic as embrittled tungsten wire shows a large scatter in strength [7].

Using the shear lag model the contribution of this effect to the toughening can be calculated:

$$W_{f,po} = w^*_{f,po} \cdot {r_f}^2 \pi = \tau_f \cdot 2{h_{max}}^2 \cdot r_f \pi \tag{10}$$

with

$w^*_{f,po}$	: specific energy consumption by fibre pull-out	[J m^{-2}]
r_m	: fibre radius	[m]
τ_f	: frictional shear strength	[MPa]
h_{max}	: pull-out length	[m]

An estimation can be done by using a frictional shear strength $\tau_i = 64\,\mathrm{N\,mm^{-2}}$ determined experimentally in investigations by Du [22] leading to $w^*_{f,po,64} = 1 \times 10^{1}\mathrm{mJ\,mm^{-2}}$. This pull-out contribution to the toughening is significantly lower than the contribution by the ductile deformation $w^*_{f,pl}$. However, the energy consumed by pull-out scales quadratically with the pull-out length. For example a pull-out length in the range of the determined debonding for the elastic bridging of 300–400 µm would lead to a consumption of energy $W_{f,po}$ in the order of 0.9–1.5 mJ (calculated with $\tau_i = 64\,\mathrm{N\,mm^{-2}}$) which is only a factor 3–5 smaller than the contribution by plastic deformation $W_{f,pl}$.

The WO_x interface does not stay intact during the heat treatment

Table 3
Extrinsic toughening in ceramics after [18].

Mechanism	Highest toughness in [MPa m$^{0.5}$]
Transformation	~ 20
Microcracking	~ 10
Metal dispersion	~ 25
Whiskers/platelets	~ 15
Fibres	≤ 30

and grain growth across the fibre-matrix-interface is observed. Thus no debonding is possible and the crack propagates through the fibre instantaneously when the matrix cracks. The crack path is similar in fibre and matrix and no debonding is detected. Therefore, no elastic or pull-out bridging is observed. No indication of any influence on the fracture toughness was observed. In summary although only one sample was tested the variety of observation techniques (mechanical behaviour, tomographic observation, and fracture surface observation) gives clear evidence that if there is no distinct interface between fibre and matrix extrinsic toughening is not working in embrittled W_f/W.

These findings for the single fibre composites can be used to estimate the influence of the extrinsic toughening mechanisms on bulk W_f/W composite material. Assuming a fibre volume fraction of 30% and a full contribution of each fibre, the contribution of respective mechanism can be estimated using Eqs. (2)–(5) (assuming plane strain conditions):

- $\Delta G_{f,pl} = 81\,\mathrm{mJ\,mm^2}$, $\Delta K_{f,pl} = 189\,\mathrm{MPa\,m^{0.5}}$
- $\Delta G_{f,br} = 0.96\,\mathrm{mJ\,mm^2}$, $\Delta K_{f,br} = 21\,\mathrm{MPa\,m^{0.5}}$
- $\Delta G_{f,po} = 2.9\,\mathrm{mJ\,mm^2}$, $\Delta K_{f,po} = 36\,\mathrm{MPa\,m^{0.5}}$

The results clearly show the intense toughening effect by ductile deformation which has been also found in tension tests [27]. The effect of pull-out is significantly lower but compared to extrinsic toughening effects in ceramics (see Table 3) still high. There is a significant contribution by elastic bridging which will be active both in the as-fabricated and embrittled case. However, it is more effective in the later one due to the overall lower toughness level. Comparing the toughening induced by ductile deformation or by elastic bridging it is interesting to note that the difference does not necessarily come from the lower fracture strength but from the lower fracture strain. Regarding pull-out the debonding length and the frictional shear strength determine the toughening. This estimation is, of course, a simplified first approximation of the toughening contribution in bulk W_f/W, which is likely to be different in reality. The estimation assumes a full contribution of the above-described mechanism for each fibre. For ductile deformation this is only the case if each fibre extends by 90 μm (which is normally not the case in a real structure). In the embrittled case it is not likely that each fibre contributes in the same way as fracture follows a statistically distribution regarding strength and location. Also multiple cracking as observed in [55] might occur and change the situation. This was discussed in detail elsewhere [27].

6. Conclusion and outlook

The contribution of different mechanisms to the toughness of tungsten fibre-reinforced tungsten composites has been investigated by means of in-situ mechanical tests monitored by synchrotron X-ray tomography. Bending tests on single fibre composite systems allowed a quantitative estimation and the comparison to analytical models. Mechanical testing in combination with synchrotron tomography allowed to draw conclusions for which future experiments can give additional confirmation.

The main conclusion is that mechanisms with a significant contribution to the toughness are active in both as-fabricated and embrittled state of W_f/W. Also in the embrittled case there is a significant contribution of elastic bridging and pull-out to the toughness. Especially the first one could only have been revealed by the in-situ tomographic observation as elastic bridging is only active for a short time during the cracking process. In addition, the role of the fibre/matrix interface was investigated by testing samples with a weak interface and a stable interface, respectively. In the as-fabricated case the interface type does not play a significant role. In the embrittled case extrinsic mechanisms of toughening are only active if the interface stays intact. The results give hope that W_f/W can retain toughness even when expiring operational embrittlement of its components and can therefore contribute to solve this major problem for the use of tungsten in a fusion reactor.

The investigations showed that the real stress state and the real debonding situation are essential for analyzing the activation of the mechanisms and for an estimation of their actual contribution. Longitudinal sections combined with SEM observation are planned analyze the debonding with higher resolution and allow a comparison to the tomography results. Further Mechanical tests in combination with high energy synchrotron tomography and diffraction are planned to investigate the stress-state in detail. In addition tests on multi-fibre samples should allow to understand the correlation of single fibre effects and the overall toughness of bulk W_f/W material.

Acknowledgments

At first we want to thank the European Sychrotron Radiation Facility for granting beamtime and the beamline staff of ID15 for their assistance in performing the experiments. We also thank P. Hahn, S. Kimmig and M. Köppen who contributed by their experimental assistance during the synchrotron experiments significantly to the success of this investigation. We thank J. Du and G. Matern for the thorough preparation of metallographical sections. We acknowledge support by Osram GmbH, Schwabmünchen, Germany for providing the tungsten wire and Archer Technicoat Ltd, High Wycombe, UK for the CVD production. For their assistance in applying and setting up a tomography experimental campaign we want to thank the Riso National Lab and representative S.F. Nielsen and H.F. Poulsen. This work was supported by EURATOM and was partly carried out within the Seventh Framework Program (Grant Agreement 224752). The views and opinions expressed herein do not necessarily reflect those of the European Commission.

Appendix A. Contribution by elastic bridging considering a frictional component

Eq. (4) is based on the description given by Becher [40] however we use a factor of 3 compared to his work (see his Eq. (10b)). In the following we describe the reason for this difference. In his approach, he describes the stress along one fibre $\sigma_f(y)$ using the shear lag theory:

$$\begin{aligned}\sigma_f(y) &= 2r\pi(u_{db} - y)\cdot\tau\frac{1}{r_f^2\pi}\\ \sigma_{f,max}(y=0) &= \frac{2u_{db}\tau}{r}\end{aligned} \tag{A.1}$$

Where y is the distance from the crack surface along the fibre. What leads to:

$$u_{db} = \frac{\sigma_{f,max} r}{2\tau} \tag{A.2}$$

He uses following relation for the fibre strain:

$$\epsilon_f = \frac{u}{u_{db}} = \frac{\sigma_f}{E} \tag{A.3}$$

to determine the crack opening u as follows:

$$u = \frac{\sigma_f}{E} \cdot u_{db} \tag{A.4}$$

Using this and Eq. (A.2) leads to following relation:

$$u = \frac{2u_{db}^2 \tau}{Er} = \frac{r(\sigma_f)^2}{2E\tau} \tag{A.5}$$

In contrast to the derivation in [40], there is a factor of 2 difference which leads following his evaluation to the mentioned difference in Eq. (4).

Appendix B. Upright 4-point bending test: geometrical relations

Using the geometrical relations of the setup given in Fig. 2 the tension force and displacement can be transferred to the corresponding bending and deflection values. The bending moment M_b is calculated as

$$M_b = F_z \cdot X$$
$$M_b = \frac{F_b}{2} \cdot x$$

and with that

$$F_b = \frac{2X}{x} F_z \tag{B.1}$$

with

F_z	: tensile force	[N]
F_b	: bending force	[N]
X	: length lever arm 1	[m]
x	: length lever arm 2	[m]

The length of the lever arm 1 is determined by the thickness of the sample and is therefore determined for each sample seperately before the test ($X = 9.75$ mm in a rectangular configuration for a sample diameter of 1.5 mm). The length of the lever arm 2 is $x = 3$ mm.

By using the moment of inertia for a cylinder of $I_y = (\pi r^4)/4$ the stress σ_n at the notch can be calculated as follows (the contribution of the notch on the moment of inertia is neglected):

$$\sigma_n = \frac{8F_z X \cdot (r - a)}{\pi r^4} \tag{B.2}$$

with

a	: notch length	[m]
r	: radius at notch	[m]

The deflection of the specimen at the inner load transmission points δ^* and at the notch δ is calculated with the following consideration:

$$\frac{\frac{\Delta z}{2}}{X} = \sin\alpha = \frac{\delta^*}{x}$$

and thus

$$\delta^* = \frac{\Delta z x}{2X}$$
$$\delta = \frac{\Delta z (l + 2x)}{4X} \tag{B.3}$$

with

δ^*	: deflection at inner load transmission point	[m]
δ	: deflection at notch	[m]
Δz	: vertical displacement	[m]
l	: distance between inner pins	[m]

References

[1] N. Baluc, Final report on the EFDA Task TW1-TTMA-002 Deliverable 5, Technical Report, Centre de Recherches en Physique de Plasmas, 2002.
[2] J.W. Coenen, S. Antusch, M. Aumann, W. Biel, J. Du, J. Engels, S. Heuer, A. Houben, T. Hoeschen, B. Jasper, F. Koch, J. Linke, A. Litnovsky, Y. Mao, R. Neu, G. Pintsuk, J. Riesch, M. Rasinski, J. Reiser, M. Rieth, A. Terra, B. Unterberg, T. Weber, T. Wegener, J.-H. You, Ch. Linsmeier, Materials for demo and reactor applications – boundary conditions and new concepts, Phys. Scr. T167 (2016). 014002 (11pp)
[3] J. Davis, V. Barabash, A. Makhankov, L. Plöchl, K. Slattery, Assessment of tungsten for use in the ITER plasma facing components, J. Nucl. Mater. 258–263, Part 1 (1998) 308–312.
[4] E. Lassner, W.-D. Schubert, Tungsten – Properties, Chemistry, Technology of the Element, Alloys, and Chemical Compounds, Kluwer Academic/Plenum Publishers, 1999.
[5] J. Reiser, M. Rieth, B. Dafferner, A. Hoffmann, Charpy impact properties of pure tungsten plate material in as-received and recrystallized condition (1h at 2000°C(2273k)), J. Nucl. Mater. 442 (2013) S204–S207.
[6] J. Riesch, Y. Han, J. Almanstötter, J.W. Coenen, T. Höschen, B. Jasper, P. Zhao, C. Linsmeier, R. Neu, Development of tungsten fibre-reinforced tungsten composites towards their use in DEMO – potassium doped tungsten wire, Phys. Scr. T167 (2016). 014006 (8pp)
[7] P. Zhao, J. Riesch, T. Höschen, J. Almannstötter, M. Balden, J. Coenen, R. Himml, W. Pantleon, U. von Toussaint, R. Neu, Microstructure, mechanical behavior and fracture of pure tungsten wire after different heat treatments, Int. J. Refract. Met. Hard Mater 68 (2017) 29–40.
[8] S. Yih, C. Wang, Tungsten: Source, Metallurgy, Properties, and Applications, Springer Science + Business Media New York, 1979.
[9] J. Steichen, Tensile properties of neutron irradiated TZM and tungsten, J. Nucl. Mater. 60 (1) (1976) 13–19.
[10] S. Maloy, M. James, W. Sommer, G. Willcut, M. Lopez, T. Romero, M. Toloczko, The effect of 800 MeV proton irradiation on the mechanical properties of tungsten at room temperature and at 475°C, J. Nucl. Mater. 343 (2005) 219–226.
[11] M. Rieth, S. Dudarev, S. Gonzalez de Vicente, J. Aktaa, T. Ahlgren, S. Antusch, A. D.E.J., M. Balden, N. Baluc, M.-F. Barthe, W. Basuki, M. Battabyal, C. Becquart, D. Blagoeva, H. Boldyryeva, J. Brinkmann, M. Celino, L. Ciupinski, J. Correia, A. Debacker, C. Domain, E. Gaganidze, C. García-Rosales, J. Gibson, M. Gilbert, S. Guisepponi, B. Gludovatz, H. Greuner, K. Heinola, T. Höschen, A. Hoffmann, N. Holstein, F. Koch, W. Krauss, H. Li, S. Lindig, J. Linke, C. Linsmeier, H. Maier, J. Matejicek, T. Mishra, M. Muhammed, A. Mu?oz, M. Muzyk, K. Nordlund, D. Nguyen-Manh, J. Opschoor, T. Palacios, G. Pintsuk, R. Pippan, J. Reiser, J. Riesch, S. Roberts, M. Rosinski, M. Sanchez, W. Schulmeyer, H. Traxler, A. Urena, J. van der Laan, L. Velva, S. Wahlberg, M. Walter, T. Weber, T. Weitkamp, S. Wurster, M. Yar, J.-H. You, A. Zivelonghi, further members of EFDA Topical Group on Materials, Recent progress in research on tungsten materials for nuclear fusion applications in europe, J. Nucl. Mater. 432 (2013) 482–500.
[12] S. Wurster, N. Baluc, M. Battabyal, T. Crosby, J. Du, C. García-Rosales, A. . Hasegawa, A. Hoffmann, A. Kimura, H. Kurishita, R. Kurtz, H. Li, J. Reiser, J. Riesch, M. Rieth, W. Setyawan, M. Walter, J.-H. You, R. Pippan, Recent progress in R&D on tungsten alloys for divertor structural and plasma facing materials, J. Nucl. Mater. 442 (2013) S181–S189.
[13] A. Evans, Overview no. 125: design and life prediction issues for high-temperature engineering ceramics and their composites, Acta Mater. 45 (1997) 23–40.
[14] M. Launey, R. Ritchie, On the fracture toughness of advanced materials, Adv. Mater. 21 (2009) 2103–2110.
[15] R. Ritchie, Mechanisms of fatigue crack propagation in metals, ceramics and composites: role of crack tip shielding, Mater. Sci. Eng. A 103 (1988) 15–28.
[16] K. Chawla, Ceramic Matrix Composites, Chapman & Hall, 1993.
[17] R. Jones, C. Henager Jr., Subcritical crack growth processes in SiC/SiC ceramic matrix composites, J. Eur. Ceram. Soc. 25 (2005) 1717–1722.
[18] A. Evans, Perspective on the development of high-toughness ceramics, J. Am. Ceram. Soc. 73 (1990) 187–206.
[19] D. Hull, T. Clyne, An Introduction to Composite Materials, Cambridge University Press, 1996.
[20] J. Aveston, G.A. Cooper, A. Kelly, Proceedings of the Conference on the Properties of Fibre Composites, IPC Science & Technology Press, pp. 15–26.
[21] R. Steinbrech, Toughening mechanisms for ceramic materials, J. Eur. Ceram. Soc. 10 (1992) 131–142.
[22] J. Du, A feasibility study of tungsten-fiber-reinforced tungsten composites with engineered interfaces, Technische Universität München, 2011 Ph.D. thesis.
[23] J. Riesch, Entwicklung und Charakterisierung eines wolframfaserverstärkten Wolfram-Verbundwerkstoffs, Technische Universität München, 2012 Ph.D. thesis.
[24] J. Du, T. Höschen, M. Rasinski, S. Wurster, W. Grosinger, J.-H. You, Feasibility study of a tungsten wire reinforced tungsten matrix composite with ZrO_x interfacial coatings, Compos. Sci. Technol. 70 (2010) 1482–1489.
[25] J. Riesch, M. Aumann, J.W. Coenen, H. Gietl, G. Holzner, T. Höschen, P. Huber, M. Li, C. Linsmeier, R. Neu, Chemically deposited tungsten fibre-reinforced tungsten – the way to a mock-up for divertor applications, Nuclear Mater. Energy 9 (2016) 75–83.
[26] Ch. Linsmeier, M. Rieth, J. Aktaa, T. Chikada, A. Hoffmann, J. Hoffmann, A. Houben, H. Kurishita, X. Jin, M. Li, A. Litnovsky, S. Matsuo, A. Müller, V. Nikolic, T. Palacios, R. Pippan, D. Qu, J. Reiser, J. Riesch, T. Shikama, R. Stieglitz, T. Weber, S. Wurster, J.-H. You, Z. Zhou, Development of advanced high heat flux and plasma-facing materials, Nucl. Fusion 57 (2016). 092007 (60pp)
[27] J. Riesch, J.-Y. Buffiere, T. Höschen, M. di Michiel, M. Scheel, Ch. Linsmeier, J.-H. You, In situ synchrotron tomography estimation of toughening effect by semi-ductile fibre reinforcement in a tungsten-fibre-reinforced tungsten composite system, Acta Mater. 61 (19) (2013) 7060–7071.
[28] J. Riesch, T. Höschen, Ch. Linsmeier, S. Wurster, J.-H. You, Enhanced toughness and stable crack propagation in a novel tungsten fibre-reinforced tungsten composite produced by chemical vapour infiltration, Phys. Scr. 2014 (T159) (2014). 014031 (7pp)
[29] R. Neu, J. Riesch, J. Coenen, J. Brinkmann, A. Calvo, S. Elgeti, C. Garcá-Rosales, H. Greuner, T. Höschen, G. Holzner, F. Klein, F. Koch, Ch. Linsmeier, A. Litnovsky, T. Wegener, S. Wurster, J.-H. You, Advanced tungsten materials for plasma-facing components of DEMO and fusion power plants, Fusion Eng. Des. 109–111 (PartA) (2016) 1046–1052.
[30] D.L. McDanels, Tungsten Fiber reinforced copper matrix composites, NASA Technical Paper 2924, NASA, 1989. accessed 2016
[31] D. Petrasek, R. Signorelli, Tungsten fiber reinforced superalloys – a status review, Technical Memorandum, NASA, 1981.
[32] J. Hill, F. Banta, Characterization of wire-wound tungsten composite, Technical Report, United Technology Centre, 1972.
[33] J. Murphy, A. Giannattasio, Z. Yao, C. Hetherington, P. Nellist, S. Roberts, The mechanical properties of tungsten grown by chemical vapour deposition, J. Nucl. Mater. 386–388 (2009) 583–586.
[34] J.Y. Buffiere, P. Cloetens, W. Ludwig, E. Maire, L. Salvo, In situ x-ray tomography studies of microstructural evolution combined with 3D modelling, MRS Bull. 33 (2008) 611–619.
[35] M. Preuss, G. Rauchs, P.J. Withers, E. Maire, J.-Y. Buffière, Interfacial shear strength of Ti/SiC fibre composites measured by synchrotron strain measurement, Compos. Part A Appl. Sci. Manuf. 33 (2002) 1381–1385.
[36] Y.-C. Hung, J. Bennett, F. Garcia-Pastor, M. Di Michiel, J.-Y. Buffière, T. Doel, P. Bowen, P. Withers, Fatigue crack growth and load redistribution in Ti/SiC composites observed in situ, Acta Mater. 57 (2009) 590–599.
[37] Y.C. Hung, P.J. Withers, Fibre bridging during high temperature fatigue crack growth in Ti/SiC composites, Acta Mater. 60 (3) (2012) 958–971.
[38] P.J. Withers, J.A. Bennett, M. Kuroda, Interfacial shear strength behaviour of Ti/SiC metal matrix composites at room and elevated temperature, Acta Mater. 58 (18) (2010) 6090–6103.
[39] T. Anderson, Fracture Mechanics: Fundamentals and Applications, Taylor & Francis Group LLC, 2005.
[40] P.F. Becher, Microstructural design of toughened ceramics, J. Am. Ceram. Soc. 74 (2) (1991) 255–269.
[41] M. Ashby, F. Blunt, M. Bannister, Flow characteristics of highly constrained metal wires, Acta Metall. 37 (1989) 1847–1857.
[42] J.-K. Kim, Y.-W. Mai, Engineered Interfaces in Fiber Reinforced Composites, Elsevier Science Ltd., 1998.
[43] M. Preuss, P.J. Withers, E. Maire, J.-Y. Buffière, SiC single fibre full-fragmentation during straining in a Ti-6Al-4V/SiC matrix studied by synchrotron x-rays, Acta Mater. 50 (2002) 3175–3190.
[44] A.F. Zinn, Chemical vapor depositon of tungsten, in: T. Kodas, M. Hampden-Smith (Eds.), The Chemistry of Metal CVD, VCH Verlagsgesellschaft mbH, 1994, pp. 105–174.
[45] A. Manhard, M. Balden, S. Elgeti, Quantitative microstructure and defect density analysis of polycrystalline tungsten reference samples after different heat treatments, PM 52 (8) (2015) 437–466.
[46] J. Riesch, Ch. Linsmeier, S.F. Nielsen, In-situ tomographic observation of crack formation and propagation in tungsten materials in the framework of FEMaS-CA, Proceedings of the Thirty-first Riso International Symposium on Materials Science: Challenges in Materials Science and Possibilities in 3D and 4D Characterization Techniques, (2010), pp. 405–412. Roskilde, Denmark
[47] M. Altschuler, R. Bracewell, T. Biudinger, B. Gilber, G. Gullberg, L. Harris, G. Herman, R. Huseman, J. Kinsey, R. Lewitt, E. Ritman, R. Robb, S. Rowland, E.H. Wood, Image Reconstruction from Projections, Springer Verlag, 1979.
[48] Fiji, http://fiji.sc/Fiji (2015).
[49] J.-Y. Buffiere, E. Maire, J. Adrien, J.-P. Masse, E. Boller, In situ experiments with x-ray tomography: an attractive tool for experimental mechanics, Exp. Mech. 50 (3) (2010) 289–305–.
[50] J.B. Wachtman, Mechanical Properties of Ceramics, John Wiley & Sons, Inc., 1996.
[51] J. Leber, J. Tavernelli, D. White, R. Hehemann, Fracture modes in tungsten wire, J. Less-Common Met. 48 (1976) 119–133.
[52] J. Riesch, J. Almanstötter, J.W. Coenen, M. Fuhr, H. Gietl, Y. Han, T. Höschen, C. Linsmeier, N. Travitzky, P. Zhao, R. Neu, Properties of drawn w wire used as high performance fibre in tungsten fibre-reinforced tungsten composite, IOP Conf. Ser. Mater. Sci. Eng. 139 (1) (2016). 012043 (9pp)
[53] W. Weibull, A statistical theory of the strength of materials, Royal Swedish Academy Eng. Sci. 151 (151) (1939).
[54] N. Pan, H. Chen, J. Thompson, M. Inglesby, S. Khatua, X. Zhang, S. Zeronian, The size effects on the mechanical behaviour of fibres, J. Mater. Sci. 32 (10) (1997) 2677–2685.
[55] H. Gietl, J. Riesch, J. Coenen, T. Höschen, C. Linsmeier, R. Neu, Tensile deformation behavior of tungsten fibre-reinforced tungsten composite specimens in as-fabricated state, Fusion Eng. Des. 124 (2017) 396–400.